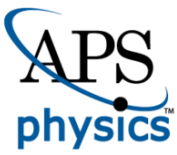

Ultrafast Suppression of the Ferroelectric Instability in math xmlns="http://www.w3.org/1998/Math/MathML" display="inline">mrow>msub>mrow>mi>KTaO/mi>/mrow >mrow>mn>3/mn>/mrow>/msub>/mrow>/math>

Viktor Krapivin, Mingqiang Gu, D. Hickox-Young, S. W. Teitelbaum, Y. Huang, G. de la Peña, D. Zhu, N. Sirica, M.-C. Lee, R. P. Prasankumar, A. A. Maznev, K. A. Nelson, M. Chollet, James M. Rondinelli, D. A. Reis, and M. Trigo

Phys. Rev. Lett. **129**, 127601 — Published 14 September 2022

DOI: 10.1103/PhysRevLett.129.127601

Ultrafast Suppression of the Ferroelectric Instability in $KTaO_3$

Viktor Krapivin,[1,2,3,*] Mingqiang Gu,[4] D. Hickox-Young,[4] S. W. Teitelbaum,[1,2] Y. Huang,[1,2,3] G. de la Peña,[1,2] D. Zhu,[5] N. Sirica,[6] M.-C. Lee,[6] R. P. Prasankumar,[6] A. Maznev,[7] K. A. Nelson,[7] M. Chollet,[5] James M. Rondinelli,[4,2] D. A. Reis,[1,2,3] and M. Trigo[1]

[1] *Stanford PULSE Institute, SLAC National Accelerator Laboratory, Menlo Park, California 94025, USA*
[2] *Stanford Institute for Materials and Energy Sciences, SLAC National Accelerator Laboratory, Menlo Park, California 94025, USA*
[3] *Department of Applied Physics, Stanford University, Stanford, California 94305, USA*
[4] *Department of Materials Science and Engineering, Northwestern University, Evanston, Illinois 60208, USA*
[5] *Linac Coherent Light Source, SLAC National Accelerator Laboratory, Menlo Park, California 94025, USA*
[6] *Center for Integrated Nanotechnologies, Los Alamos National Laboratory, Los Alamos, New Mexico 87545, USA*
[7] *Department of Chemistry, Massachusetts Institute of Technology*

(Dated: July 25, 2022)

We use an x-ray free-electron laser to study the lattice dynamics following photoexcitation with ultrafast near-UV light (wavelength 266 nm, 50 fs pulse duration) of the incipient ferroelectric potassium-tantalate, $KTaO_3$. By probing the lattice dynamics corresponding to multiple Brillouin zones through the x-ray diffuse scattering with pulses from the Linac Coherent Light Source (LCLS) (wavelength 1.3 Å and < 10 fs pulse duration), we observe changes in the diffuse intensity associated with a hardening of the transverse acoustic phonon branches along Γ to X and Γ to M. Using force constants from density functional theory (DFT), we fit the quasi-equilibrium intensity and obtain the instantaneous lattice temperature and density of photoexcited charge carriers. The DFT calculations demonstrate that photoexcitation transfers charge from oxygen $2p$ derived π-bonding orbitals to Ta $5d$ derived antibonding orbitals, further suppressing the ferroelectric instability and increasing the stability of the cubic, paraelectric structure.

Understanding the interplay between a material structure and its functionality is paramount to devising new technologies. This relationship is evidenced clearly in transition metal oxides (TMO) where multiple strongly interacting degrees of freedom (spin, charge, lattice) give rise to rich phases separated by small energy barriers resulting in giant material responses to external stimuli such as fields or pressure [1]. Within TMOs, the ABO_3 cubic perovskite structure is the building block for many important materials such as ferroelectrics and multiferroics [2–5], with multiple competing phases influenced by particular electronic state configurations [6–8] as well as anharmonic interactions[9]. New strategies for realizing novel phases and functionality can be devised from understanding how microscopic structural and electronic features, e.g., spontaneous polarizations, can be modified by light pulses.

In the non-equilibrium state, our understanding of the behavior of coupled electrons and lattice at ultrafast timescales is limited, in part because of the lack of ultrafast atomic-scale probes of the photoexcited material. X-ray free electron lasers (XFEL)s [10–14] enable probing of coupled electron and lattice degrees of freedom with Ångstrom wavelengths and at sub-picosecond timescales. Recent experiments using XFELs in $EuTiO_3$ and doped $SrTiO_3$ find strong modifications of the interatomic potential upon photoexcitation [8, 15]. However, these measurements were limited to the Bragg peak response, and thus provide information about the average crystal unit cell. In contrast, the x-ray diffuse intensity *between* Bragg peaks [16] can be used to visualize the evolution of the fluctuations. Notably, ultrafast x-ray diffuse scattering is sensitive to nonequilibrium lattice dynamics, including phonons with wavevectors across reciprocal space, and thus can be used to obtain the transient interatomic potential and corresponding forces in the photoexcited state [17]. This approach provides new insights into structural transitions [18, 19].

Here we study $KTaO_3$, which is the structurally simplest member of a broad class of materials based on the ABO_3 perovskite structure. This parent structure leads to multitude of instabilities that may involve oxygen octahedra rotations (e.g. $SrTiO_3$), and/or off-centering of the A or B ions (e.g., $BaTiO_3$ and $PbTiO_3$) [20]. The resulting effective anharmonic interaction between these structural distortions may be the key to novel materials with ferroelectric [20] or multiferroic orders [2, 21]. Earlier neutron scattering work on $KTaO_3$ revealed a softening of the lowest (at Γ) transverse optical (TO) and transverse acoustic (TA) phonon branches at low temperatures along $\Gamma - X - M - \Gamma$, suggesting a coupling between these branches. The zone-center TO mode is identified as the ferroelectric mode [22, 23], which softens at low temperature. However, the material does not become ferroelectric at finite temperature, presumably due to quantum lattice fluctuations [24]. $KTaO_3$ is a quantum paraelectric material similar to $SrTiO_3$ [25], yet simpler, as $KTaO_3$ remains cubic to very low temperatures [26]. Here we find a stiffening of the phonon branches upon photoexcitation through a decrease in the diffuse x-ray intensity. Using

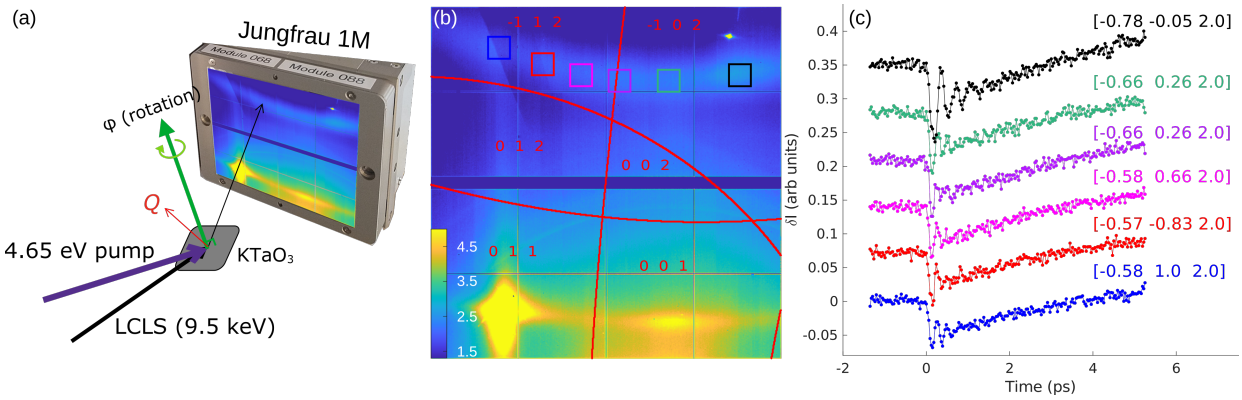

FIG. 1. (a) Schematic of the grazing incidence scattering geometry. Pump and probe are represented by purple and black arrows, respectively. The scattered x rays are collected with an area detector positioned 110 mm from the sample. The momentum transfer $\mathbf{Q}$ is shown schematically. The axis of ϕ rotation is parallel to the sample normal and $\phi = 0$ corresponds to the (100) direction parallel to the incident x ray beam. (b) Room temperature diffuse scattering pattern from $KTaO_3$ for $\phi = 16.98°$. The red lines and labels show the boundaries between Brillouin zones and the corresponding reciprocal lattice indices. The scale bar represents linear intensity scale in arbitrary units. (c) time dependence of the intensity averaged over each box indicated in (b). The labels indicate the reduced wavevector of the center of each box in reciprocal lattice units.

DFT we find that this is caused by depopulating bonding orbitals hybridized between O $2p$ and Ta $5d$. This stiffening of transverse phonons leads to a reduction of the ferroelectric instability in this broad class of materials with $p - d$ hybridized orbitals.

We use ultrafast hard x-ray diffuse scattering at the Linac Coherent Light Source (LCLS) x-ray free electron laser to probe the dynamics of the $KTaO_3$ lattice over a wide range of momentum space upon above-band-gap photoexcitation with 4.65 eV photons. We treat the lattice with an effective time-dependent temperature after $\sim$ 1 ps, and we fit the changes to the diffuse intensity with the phonons calculated from interatomic forces constants (IFCs) from density functional theory (DFT), see Supplemental Material for details. We interpret the reduction in diffuse scattering as due to a stiffening of the low frequency TA mode, which is associated with a further stabilization of the cubic phase away from the incipient ferroelectric state.

The laser-pump, x ray-probe experiment was conducted at the LCLS X-ray Pump Probe (XPP) station [10, 27, 28] using x ray pulses < 10 fs in duration with a probe (pump) photon energy of 9.5 keV (4.65 eV). The pump and probe spot sizes on the sample surface were $0.2 \times 2.5\,\mathrm{mm}^2$ and $0.2 \times 1.6\,\mathrm{mm}^2$, respectively, see Figure 1a. The pump was p-polarized with an incident fluence of 6 $\mathrm{mJ/cm}^2$. Additional details can be found in the Supplemental Material.

Figure 1b shows the static x-ray diffuse scattering pattern from a (001)-oriented single crystal of $KTaO_3$ at room temperature. The detector covers multiple Brillouin zones (BZ)s of the cubic structure, labeled by their corresponding indices in Figure 1b. Broad vertical and horizontal bands are apparent in the diffuse intensity; these originate from thermal diffuse scattering [29] from the soft TA phonon branches in $KTaO_3$ primarily along the Γ to X and Γ to M directions [24, 30]. Additionally, static disorder within the sample, Compton, and air scattering can contribute a broad diffuse background. Figure 1c shows the time-dependence of the intensity integrated over the colored boxes indicated in Figure 1b, which span between the $(\bar{1}\ 1\ 2)$ and $(\bar{1}\ 0\ 2)$ BZs. The path spanned by these regions of interest approximately follows X to M in reciprocal space. We observe a sudden intensity *decrease* followed by damped oscillations over a wide range of wavevectors. These oscillations originate from squeezed phonons caused by a sudden change in the phonon frequencies, which acts as a sudden parametric excitation[31]. The resulting motion modulates the squared displacements $\langle u^2(\mathbf{Q}, t)\rangle$, where $u(\mathbf{Q})$ is the mode amplitude at momentum transfer $\mathbf{Q}$ and the brackets denote a thermal average [16, 19, 32, 33]. The intensity here oscillates at twice the frequency of the lowest TA branch and the speed of the initial decrease is comparable to $\sim 1/4$ of the phonon period[32]. While these oscillations could be used to extract the frequency of the modes [19] and, consequentially, the non-equilibrium IFCs [17], the fast decay in our case results in poor frequency resolution and reduced sensitivity to the forces. Instead, we focus on the non-oscillatory dynamics in Figure 1c, which can also be related to the IFCs [34]. The initial decrease in the diffuse intensity is unusual, since generally the pump would increase rather than decrease the diffuse intensity by raising the effective lattice temperature [15, 16, 18]. Instead, a *decrease* of intensity is indicative of phonon hardening [19]. Unlike in semiconductors[19], here this change arises from a change to the occupation of d-electrons and involves the pseudo-Jahn-Teller effect[21], as we explain later in this text.

We begin by extending the equilibrium expression for the thermal diffuse scattering intensity [29, 35] to a time-

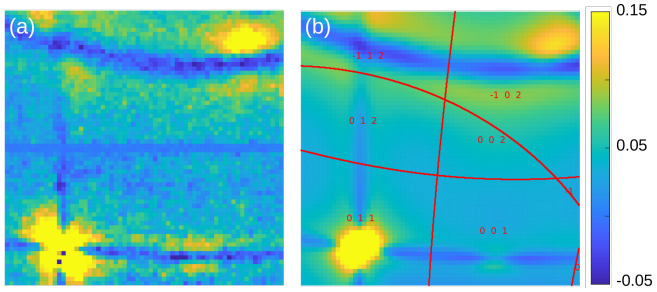

FIG. 2. (a) experimentally measured and (b) fitted $\Delta I(\mathbf{Q}, t = 3\,\text{ps})$. $\Delta I(\mathbf{Q}, t)$ in (b) was calculated for $\rho = 0.08$ electrons per unit cell and $T = 480\,\text{K}$ (see text for details). The intensity scale is the same as in Figure 1b.

dependent quasi-equilibrium situation. We approximate the instantaneous (incoherent) phonon populations that give rise to non-oscillatory intensity in Figure 1 as described by a time-dependent lattice temperature T and instantaneous frequencies. The mode frequencies and displacements are obtained from the eigenvalues and eigenvectors of the (transient) dynamical matrix, which depends parametrically on the density of photoexcited carriers (electrons and holes), ρ, that varies slowly with time. Under these assumptions the intensity at a time t and momentum transfer $\mathbf{Q}$,

$$I(\mathbf{Q}, t) = C \sum_j \frac{1}{\omega_{j,\mathbf{q}}} \coth\left(\frac{\hbar\omega_{j,\mathbf{q}}}{2k_B T}\right) |F_j(\mathbf{Q})|^2 \quad (1)$$

$$F_j(\mathbf{Q}) = \sum_s \frac{f_s}{\sqrt{\mu_s}} \exp(-M_s)(\mathbf{Q} \cdot \mathbf{e}_{q_{j,s}}), \quad (2)$$

here T is the time-dependent lattice temperature; $\mathbf{q} = \mathbf{Q} - \mathbf{K}$ is the reduced wavevector, where $\mathbf{K}$ is the closest reciprocal lattice vector to $\mathbf{Q}$; $\omega_{j,\mathbf{q}}$ is the frequency of branch j at wavevector $\mathbf{q}$, $\mathbf{e}_{q,j,s}$ is the eigenvector component of the s-th atom in the unit cell for the j-th vibrational mode at $\mathbf{q}$. M_s is the Debye-Waller factor, μ_s is the mass and f_s is the atomic scattering factor of the s-th atom in a unit cell, respectively; C is a constant. The quantities $\omega_{j,\mathbf{q}}$ and $\mathbf{e}_{q,j,s}$ are implicitly functions of ρ through the IFCs[16, 29, 35]. Finally, to compare with experiment we consider the change in intensity

$$\Delta I(\mathbf{Q}, t) = I(\mathbf{Q}, t) - I(\mathbf{Q}, t < 0), \quad (3)$$

where $I(\mathbf{Q}, t < 0)$ is the x ray intensity recorded with the pump arriving after the probe, which is very similar to the equilibrium pattern in Figure 1b.

While a rapid increase in $\Delta I(\mathbf{Q}, t)$ may be a signature of an increase in the phonon population (described by the temperature in our approximation), the fast ~ 100 fs initial decrease in the intensity in Figure 1c is too fast to be sudden cooling of the lattice. Instead, we attribute this fast decrease in $\Delta I(\mathbf{Q}, t)$ to an *increase* in the phonon frequency (Equation 1) caused by a modification of the IFCs by the photoexcited ρ. This is consistent with the initial phase of the oscillations. Thus, we describe the dynamics shown in Figure 1c using (Equation 1-Equation 3) where the phonon frequencies are obtained from DFT and we assume an instantaneous $\rho(t)$ at each time point. We allow the temperature to vary with time in order to capture the increase in overall intensity due to thermal effects at later times. The photoexcited state is approximated in the DFT calculation by constraining the density of electrons (holes) in the conduction (valence) band, ρ [36]. Changes in ρ modify the IFCs and the corresponding dynamical matrix, from which we obtain the frequencies and eigenvectors in (Equation 1). Importantly, a differential negative change in the intensity must originate from changes in the forces through the electron density, ρ. The dynamical matrix is obtained from force constants computed in a $2\times2\times2$ supercell for $\rho = 0$, 0.05 and 0.10. The forces were interpolated linearly between these values of ρ. The calculated intensity for $\rho = 0$ is in good agreement with the measured equilibrium intensity Figure 1b and the known phonon dispersion for the TA and lowest TO branch of $KTaO_3$ [24], as shown in Figure 3b (blue curve). Since the dominant contribution to the $I(\mathbf{Q}, t)$ is from low frequency TA modes, we did not consider LO-TO splitting. This does not affect the computed patterns significantly.

As mentioned above, to describe the non-equilibrium diffuse patterns, we assume that ρ, $\omega_{j,\mathbf{q}}$ and T in (Equation 1) are time dependent. We then extract $\rho(t)$ and $T(t)$ by fitting (Equation 1-Equation 3) to the experimental $\Delta I(\mathbf{Q}, t)$ at each time delay with $\rho(t)$, $T(t)$, and C as fitting parameters. To improve the signal to noise and since the relevant features in Figure 1b are broad in reciprocal space, we averaged the original images to 64×64 pixels. We exclude dead pixels, the region near the (0 1 1) Bragg peak, and the region near the crystal truncation rod visible in the top right of the image in Figure 1b as these features do not arise from diffuse scattering, (Equation 1), and instead are dominated by strain [37], coherent oscillations [38] or x ray beam fluctuations. The fitted and experimental $\Delta I(\mathbf{Q}, t = 3\text{ ps})$ are shown in Figure 2a and b.

The resulting $T(t)$ and $\rho(t)$ are shown in Figure 3a. Both quantities quickly rise within $t < 0.5$ ps. Afterwards, $\rho(t)$ saturates while the temperature continues to rise slowly. The agreement shown in Figure 2 indicates that, after the transient oscillations have decayed, the phonon population at $t \gtrsim 1$ ps is well parameterized by an effective temperature within the assumptions in (Equation 1). Changes in $\rho(t)$ result in time-dependent phonon frequencies that cause the slowly-varying diffuse intensity in Figure 1c after the oscillations have decayed. Thus, while we perform a fit for the entirety of our data range, we limit our interpretation of $T(t)$ as a parameterization of the phonon populations to $t > 1$ ps.

In Figure 3b, we plot the low frequency region of the

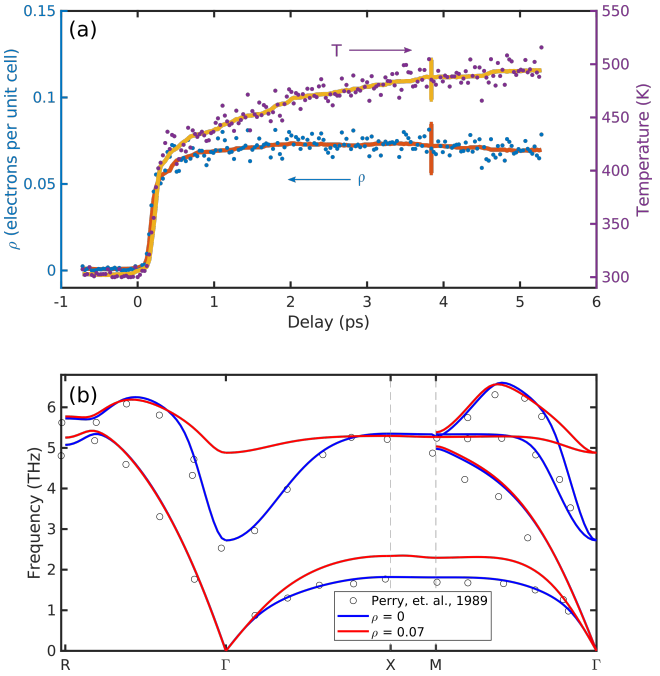

FIG. 3. (a) fitted carrier density, ρ and lattice temperature, T, for each time delay as described in the text. The error bars are representative errors obtained from the MATLAB function NLPARCI [39]. The solid lines show the median value within 30 points. (b) The low frequency part of the calculated equilibrium ($\rho = 0$) transverse phonon dispersion of $KTaO_3$ from DFT (blue line). Along the M to Γ direction the transverse branch polarized parallel to (1 $\bar{1}$ 0) and polarized parallel to (0 0 1) are plotted. Open circles represent room temperature data from neutron scattering [24]. Red trace: transient dispersion of the lowest TA/TO branches at $\rho = 0.07$ per unit cell, obtained from the fit after 1 ps.

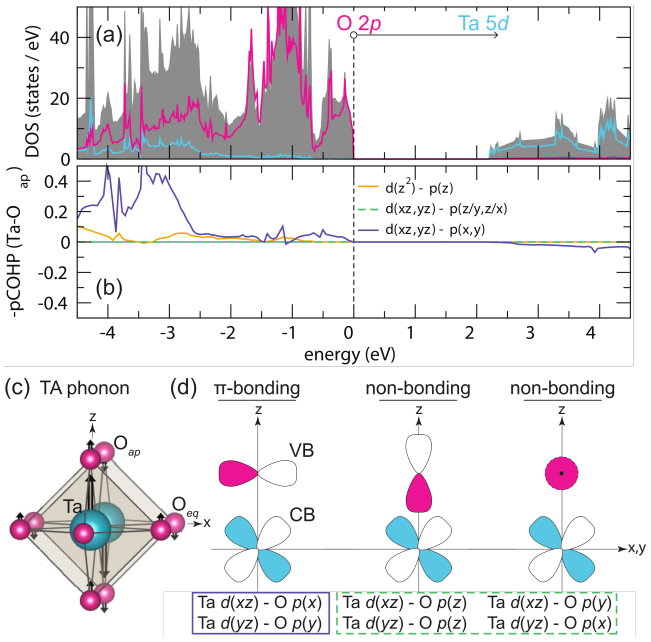

FIG. 4. (a) Calculated electron density-of-states (DOS) and (b) Projected crystal orbital Hamiltonian population (pCOHP) for Ta and the apical O atom displacing in the (c) TA mode for $KTaO_3$ at the X point with displacements indicated with black arrows in its electronic ground state. The gray filled curve corresponds to the total DOS. The horizontal arrow depicts the photoexcitation of electrons from the bonding O $2p$ states at the valence band maximum (VB) to anti-bonding Ta $5d$ states forming the conduction band (CB) as illustrated in (b). The photoexcitation indicated in (a) leads to changes in the (d) bonding interactions at the valence band maximum (VBM) to the conduction band minimum (CBM) formed by O $2p$ orbitals and Ta $5d$ t_{2g} orbitals.

phonon dispersion computed for $\rho = 0.07$ ($\rho = 0$) for the lowest two transverse branches in red (blue). At this point it is important to connect the features observed in Figure 1b and Figure 2a with the dispersion in Figure 3b. The bright lines forming a square pattern connecting the BZs in Figure 1b originate primarily from the soft TA modes along Γ-X-M shown in blue in Figure 3b. Similarly, the blue bands with $\Delta I(\mathbf{Q}, t) < 0$ in Figure 2a arise from the hardening of the TA branch along Γ-X-M as shown in Figure 3 (red curve). Also, note that the prominent hardening of the lowest TO mode near Γ is not observable in this scattering geometry (chosen to avoid the intense Bragg peaks). A direct estimate of the change in frequency based on $\Delta I(\mathbf{Q}, t)$ at $\mathbf{Q} = (-0.77,\ 0,\ 2.01)$ gives $\Delta\omega/\omega \sim 0.2 - 0.4$ after correcting for the penetration depth mismatch [40–42]. This range is consistent with $\Delta\omega/\omega = 0.2$ for $\rho = 0.07$, plotted in Figure 3b.

In the phonon dispersion shown in Figure 3b, one of the largest shifts of the TA branch is observed at the X point. This mode corresponds to the anti-polar displacements of the tantalum atoms adjacent to a neighboring unit cell shown in Figure 4c. Our DFT calculations also predict that this mode will harden with both p and n doping, see Supplemental Material for details.

To further elaborate on the mechanism of the photo-induced hardening, we consider changes in the IFCs as a function of ρ. From DFT, we find the largest changes occur in the radial component of the nearest neighbor Ta-Ta IFC by -40 eV/(Å^2 e) and the radial nearest neighbor Ta-O IFC by 12 eV/(Å^2 e) [43].

Figure 4a shows the expected insulating behavior in the electronic density of states (DOS). The charge transfer gap arises from semicovalent Ta-O interactions that produce a valence band primarily of O $2p$ character separated from a conduction band formed by mainly Ta $5d$ states. In the photo-excitation process, electrons are removed from near the valence band edge to near the conduction band edge. Figure 4b shows the negative projected crystal orbital Hamiltonian population (-pCOHP) for the apical oxygen ligand with Ta decomposed as bonding (positive COHP values), antibonding (negative), and nonbonding (zero) interactions.

We find that the states (derived from the apical oxygen,

O_{ap}, interacting with Ta) displace in the TA phonon mode at the X-point (Figure 4c) and do not significantly contribute bonding character to the valence band edge over the -2.5 to 0 eV energy range. The -2.5 to 0 eV energy range is dominated by non-bonding interactions [green dashed box in (d)] between Ta-O_{ap} (Figure 4d), because the $p(z)/p(y)$ orbitals approach the $d(xz)$ orbital along its nodes. The band edge also consists of π-bonding interactions between the four symmetry permitted O $2p(x/y)$ orbitals from equatorial O atoms (O_{eq}) with the Ta $d(xy)$ orbitals (not shown). Only two of the O_{eq} atoms weakly participate in the TA mode at the X-point (Figure 4c). σ-bonding interactions between Ta $d(z^2)$ and O_{ap} $p(z)$ appear at much lower and higher energy, and do not participate in the photoexcitation process.

The frequency of the TA branch, therefore, largely respond to occupancy changes in the symmetry permitted π-bonding (and antibonding) interactions between O_{ap} $2p(x)$ and $2p(y)$ orbitals with Ta $5d(xz)$ and $5d(yz)$ orbitals [purple box in Figure 4(d)], which appear from -4.5 to -2.5 eV (and begin at the CBM near $\sim$2.2 eV). Thus, photoexcitation with 4.65 eV photons depopulate these π bonding states and populate antibonding states that control the TA mode stiffness [21]. The light-controlled occupation of these electronic levels effectively disrupts the O_{ap} bond and reduces the orbital interaction (electron hopping). The corresponding IFC then hardens through the vibronic response.

Our findings give insight into the interaction between symmetry-lowering distortions and the associated electronic states that are coupled to the fluctuating distortions. The dynamic coupling, which is also tuned by the energy separation between the states, governs the stability of TA/TO modes in dielectrics[21]. For example, ferroelectric compounds that undergo structural transitions stabilized by the aforementioned $p-d$ cross-gap hybridization will exhibit TA/TO modes that harden upon photoexcitation. This was suggested in Refs. [44] for TO modes in ferroelectric perovskite oxides. Our analysis both accounts for this mode hardening behavior [8, 44] upon photoexcitation and also describes the opposite limit where photoexcitation should affect the vibrational branches weakly, *e.g.*, $PbTiO_3$ and $EuTiO_3$ which have 6s Pb states and Eu 4f in the low energy electronic structure.

We used ultrafast x-ray diffuse scattering to probe the dynamics of the lattice upon above-gap photoexcitation in $KTaO_3$. Our analysis of the diffuse intensity based on (Equation 1-Equation 3) and DFT allowed us to reconstruct the evolution of the transient phonon dispersion and the interatomic forces. We observe that photoexcitation induces a hardening of the TA branch due to changes in the IFCs. This change in IFCs moves $KTaO_3$ away from its incipient ferroelectric instability. Using DFT, we find that charge transfer from oxygen p-orbitals to tantalum d-orbitals that form π-bonding interactions explains the observed changes in the IFCs and the phonon dispersion. The photoexcitation of these π-bonding states causes the suppression of the Jahn-Teller-like effect and of the ferroelectric instability, which results in the stabilization of the cubic, paraelectric structure of $KTaO_3$. These results suggest that hardening of the TO/TA branches will occur in ferroelectrics with similar p-d hybridization, and perhaps less in systems where the s or f orbitals are active.

The experimental work was supported by the U.S. Department of Energy, Office of Science, Office of Basic Energy Sciences through the Division of Materials Sciences and Engineering through FWP No. 2018LANLBES16 (M.-C. L. and R. P. P.), Contract No. DE-AC02-76SF00515 (S. W. T., V. K., Y. H., GdP, M. T. and D. A. R.) and Contract No. DE-SC0019126 (A. M. and K. A. N.). Use of the LCLS was supported by the U.S. Department of Energy, Office of Science, Office of Basic Energy Sciences under Contract No. DE-AC02-76SF00515. Work at Northwestern University was supported by the U.S. Department of Energy (DOE), Office of Science, Office of Basic Energy Sciences (BES), under award no. DE-SC-0012375. N.S. gratefully acknowledges the support of the US Department of Energy through the Los Alamos National Laboratory LDRD program. The computational work used resources of the National Energy Research Scientific Computing Center (NERSC), a U.S. DOE Office of Science User Facility located at Lawrence Berkeley National Laboratory, operated under Contract No. DE-AC02-05CH11231, and at the Center for Nanoscale Materials, an Office of Science user facility, supported by the U.S. DOE, Office of Science, Office of BES, under Contract No. DE-AC02-06CH11357.

* krapivin@stanford.edu

[1] E. Dagotto, Science (New York, N.Y.) **v. 309**, pp. 257 (2005).
[2] N. A. Hill, The Journal of Physical Chemistry B **104**, 6694 (2000).
[3] S.-W. Cheong and M. Mostovoy, Nature Materials **6**, 13 (2007).
[4] R. Ramesh and N. A. Spaldin, Nature Materials **6**, 21 (2007).
[5] M. Fiebig, T. Lottermoser, D. Meier, and M. Trassin, Nature Reviews Materials **1**, 16046 (2016).
[6] A. Bhalla, R. Guo, and R. Roy, Materials Research Innovations **4**, 3 (2000).
[7] T. Birol and C. J. Fennie, Physical Review B **88**, 094103 (2013).
[8] M. Porer, M. Fechner, M. Kubli, M. J. Neugebauer, S. Parchenko, V. Esposito, A. Narayan, N. A. Spaldin, R. Huber, M. Radovic, E. M. Bothschafter, J. M. Glownia, T. Sato, S. Song, S. L. Johnson, and U. Staub, Physical Review Research **1**, 012005 (2019).
[9] J. Young, A. Stroppa, S. Picozzi, and J. M. Rondinelli, Journal of Physics: Condensed Matter **27**, 283202 (2015).

[10] P. Emma, R. Akre, J. Arthur, R. Bionta, C. Bostedt, J. Bozek, A. Brachmann, P. Bucksbaum, R. Coffee, F.-J. Decker, Y. Ding, D. Dowell, S. Edstrom, A. Fisher, J. Frisch, S. Gilevich, J. Hastings, G. Hays, P. Hering, Z. Huang, R. Iverson, H. Loos, M. Messerschmidt, A. Miahnahri, S. Moeller, H.-D. Nuhn, G. Pile, D. Ratner, J. Rzepiela, D. Schultz, T. Smith, P. Stefan, H. Tompkins, J. Turner, J. Welch, W. White, J. Wu, G. Yocky, and J. Galayda, Nature Photonics **4**, 641 (2010).

[11] T. Ishikawa, H. Aoyagi, T. Asaka, Y. Asano, N. Azumi, T. Bizen, H. Ego, K. Fukami, T. Fukui, Y. Furukawa, S. Goto, H. Hanaki, T. Hara, T. Hasegawa, T. Hatsui, A. Higashiya, T. Hirono, N. Hosoda, M. Ishii, T. Inagaki, Y. Inubushi, T. Itoga, Y. Joti, M. Kago, T. Kameshima, H. Kimura, Y. Kirihara, A. Kiyomichi, T. Kobayashi, C. Kondo, T. Kudo, H. Maesaka, X. M. Maréchal, T. Masuda, S. Matsubara, T. Matsumoto, T. Matsushita, S. Matsui, M. Nagasono, N. Nariyama, H. Ohashi, T. Ohata, T. Ohshima, S. Ono, Y. Otake, C. Saji, T. Sakurai, T. Sato, K. Sawada, T. Seike, K. Shirasawa, T. Sugimoto, S. Suzuki, S. Takahashi, H. Takebe, K. Takeshita, K. Tamasaku, H. Tanaka, R. Tanaka, T. Tanaka, T. Togashi, K. Togawa, A. Tokuhisa, H. Tomizawa, K. Tono, S. Wu, M. Yabashi, M. Yamaga, A. Yamashita, K. Yanagida, C. Zhang, T. Shintake, H. Kitamura, and N. Kumagai, Nature Photonics **6**, 540 (2012).

[12] H.-S. Kang, C.-K. Min, H. Heo, C. Kim, H. Yang, G. Kim, I. Nam, S. Y. Baek, H.-J. Choi, G. Mun, B. R. Park, Y. J. Suh, D. C. Shin, J. Hu, J. Hong, S. Jung, S.-H. Kim, K. Kim, D. Na, S. S. Park, Y. J. Park, J.-H. Han, Y. G. Jung, S. H. Jeong, H. G. Lee, S. Lee, S. Lee, W.-W. Lee, B. Oh, H. S. Suh, Y. W. Parc, S.-J. Park, M. H. Kim, N.-S. Jung, Y.-C. Kim, M.-S. Lee, B.-H. Lee, C.-W. Sung, I.-S. Mok, J.-M. Yang, C.-S. Lee, H. Shin, J. H. Kim, Y. Kim, J. H. Lee, S.-Y. Park, J. Kim, J. Park, I. Eom, S. Rah, S. Kim, K. H. Nam, J. Park, J. Park, S. Kim, S. Kwon, S. H. Park, K. S. Kim, H. Hyun, S. N. Kim, S. Kim, S.-m. Hwang, M. J. Kim, C.-y. Lim, C.-J. Yu, B.-S. Kim, T.-H. Kang, K.-W. Kim, S.-H. Kim, H.-S. Lee, H.-S. Lee, K.-H. Park, T.-Y. Koo, D.-E. Kim, and I. S. Ko, Nature Photonics **11**, 708 (2017).

[13] C. Milne, T. Schietinger, M. Aiba, A. Alarcon, J. Alex, A. Anghel, V. Arsov, C. Beard, P. Beaud, S. Bettoni, M. Bopp, H. Brands, M. Brönnimann, I. Brunnenkant, M. Calvi, A. Citterio, P. Craievich, M. Csatari Divall, M. Dällenbach, M. D'Amico, A. Dax, Y. Deng, A. Dietrich, R. Dinapoli, E. Divall, S. Dordevic, S. Ebner, C. Erny, H. Fitze, U. Flechsig, R. Follath, F. Frei, F. Gärtner, R. Ganter, T. Garvey, Z. Geng, I. Gorgisyan, C. Gough, A. Hauff, C. Hauri, N. Hiller, T. Humar, S. Hunziker, G. Ingold, R. Ischebeck, M. Janousch, P. Juranić, M. Jurcevic, M. Kaiser, B. Kalantari, R. Kalt, B. Keil, C. Kittel, G. Knopp, W. Koprek, H. Lemke, T. Lippuner, D. Llorente Sancho, F. Löhl, C. Lopez-Cuenca, F. Märki, F. Marcellini, G. Marinkovic, I. Martiel, R. Menzel, A. Mozzanica, K. Nass, G. Orlandi, C. Ozkan Loch, E. Panepucci, M. Paraliev, B. Patterson, B. Pedrini, M. Pedrozzi, P. Pollet, C. Pradervand, E. Prat, P. Radi, J.-Y. Raguin, S. Redford, J. Rehanek, J. Réhault, S. Reiche, M. Ringele, J. Rittmann, L. Rivkin, A. Romann, M. Ruat, C. Ruder, L. Sala, L. Schebacher, T. Schilcher, V. Schlott, T. Schmidt, B. Schmitt, X. Shi, M. Stadler, L. Stingelin, W. Sturzenegger, J. Szlachetko, D. Thattil, D. Treyer, A. Trisorio, W. Tron, S. Vetter, C. Vicario, D. Voulot, M. Wang, T. Zamofing, C. Zellweger, R. Zennaro, E. Zimoch, R. Abela, L. Patthey, and H.-H. Braun, Applied Sciences **7**, 720 (2017).

[14] S. Abeghyan, M. Bagha-Shanjani, G. Chen, U. Englisch, S. Karabekyan, Y. Li, F. Preisskorn, F. Wolff-Fabris, M. Wuenschel, M. Yakopov, and J. Pflueger, Journal of Synchrotron Radiation **26**, 302 (2019).

[15] M. Porer, M. Fechner, E. M. Bothschafter, L. Rettig, M. Savoini, V. Esposito, J. Rittmann, M. Kubli, M. J. Neugebauer, E. Abreu, T. Kubacka, T. Huber, G. Lantz, S. Parchenko, S. Grübel, A. Paarmann, J. Noack, P. Beaud, G. Ingold, U. Aschauer, S. L. Johnson, and U. Staub, Physical Review Letters **121**, 055701 (2018).

[16] M. Trigo, M. Fuchs, J. Chen, M. P. Jiang, M. Cammarata, S. Fahy, D. M. Fritz, K. Gaffney, S. Ghimire, A. Higginbotham, S. L. Johnson, M. E. Kozina, J. Larsson, H. Lemke, A. M. Lindenberg, G. Ndabashimiye, F. Quirin, K. Sokolowski-Tinten, C. Uher, G. Wang, J. S. Wark, D. Zhu, and D. A. Reis, Nature Physics **9**, 790 (2013).

[17] S. W. Teitelbaum, T. C. Henighan, H. Liu, M. P. Jiang, D. Zhu, M. Chollet, T. Sato, É. D. Murray, S. Fahy, S. O'Mahony, T. P. Bailey, C. Uher, M. Trigo, and D. A. Reis, Physical Review B **103**, L180101 (2021).

[18] S. Wall, S. Yang, L. Vidas, M. Chollet, J. M. Glownia, M. Kozina, T. Katayama, T. Henighan, M. Jiang, T. A. Miller, D. A. Reis, L. A. Boatner, O. Delaire, and M. Trigo, Science (New York, N.Y.) **362**, 572 (2018), https://science.sciencemag.org/content/362/6414/572.full.pdf.

[19] M. P. Jiang, M. Trigo, I. Savić, S. Fahy, É. D. Murray, C. Bray, J. Clark, T. Henighan, M. Kozina, M. Chollet, J. M. Glownia, M. C. Hoffmann, D. Zhu, O. Delaire, A. F. May, B. C. Sales, A. M. Lindenberg, P. Zalden, T. Sato, R. Merlin, and D. A. Reis, Nature Communications **7**, 12291 (2016).

[20] N. A. Benedek and C. J. Fennie, The Journal of Physical Chemistry C **117**, 13339 (2013).

[21] I. B. Bersuker, Physical Review Letters **108**, 137202 (2012).

[22] R. Comès and G. Shirane, Physical Review B **5**, 1886 (1972).

[23] R. Migoni, H. Bilz, and D. Bäuerle, Physical Review Letters **37**, 1155 (1976).

[24] C. H. Perry, R. Currat, H. Buhay, R. M. Migoni, W. G. Stirling, and J. D. Axe, Physical Review B **39**, 8666 (1989).

[25] K. A. Müller and H. Burkard, Physical Review B **19**, 3593 (1979).

[26] M. Tyunina, J. Narkilahti, M. Plekh, R. Oja, R. M. Nieminen, A. Dejneka, and V. Trepakov, Physical Review Letters **104**, 227601 (2010).

[27] M. Chollet, R. Alonso-Mori, M. Cammarata, D. Damiani, J. Defever, J. T. Delor, Y. Feng, J. M. Glownia, J. B. Langton, S. Nelson, K. Ramsey, A. Robert, M. Sikorski, S. Song, D. Stefanescu, V. Srinivasan, D. Zhu, H. T. Lemke, and D. M. Fritz, Journal of Synchrotron Radiation **22**, 503 (2015).

[28] C. Bostedt, S. Boutet, D. M. Fritz, Z. Huang, H. J. Lee, H. T. Lemke, A. Robert, W. F. Schlotter, J. J. Turner, and G. J. Williams, Reviews of Modern Physics **88**, 015007 (2016).

[29] B. E. Warren, *X-Ray Diffraction*, dover ed ed. (Dover

Publications, New York, 1990).
[30] J. D. Axe, J. Harada, and G. Shirane, Physical Review B **1**, 1227 (1970).
[31] T. Kiss, J. Janszky, and P. Adam, Physical Review A **49**, 4935 (1994).
[32] G. A. Garrett, A. G. Rojo, A. K. Sood, J. F. Whitaker, and R. Merlin, Science **275**, 1638 (1997).
[33] S. L. Johnson, P. Beaud, E. Vorobeva, C. J. Milne, É. D. Murray, S. Fahy, and G. Ingold, Physical Review Letters **102**, 175503 (2009).
[34] M. Holt, Z. Wu, H. Hong, P. Zschack, P. Jemian, J. Tischler, H. Chen, and T.-C. Chiang, Physical Review Letters **83**, 3317 (1999).
[35] R. Xu and T. C. Chiang, Zeitschrift für Kristallographie - Crystalline Materials **220**, 10.1524/zkri.2005.220.12.1009 (2005).
[36] P. Tangney and S. Fahy, Physical Review B **65**, 054302 (2002).
[37] D. A. Reis, M. F. DeCamp, P. H. Bucksbaum, R. Clarke, E. Dufresne, M. Hertlein, R. Merlin, R. Falcone, H. Kapteyn, M. M. Murnane, J. Larsson, T. Missalla, and J. S. Wark, Physical Review Letters **86**, 3072 (2001).
[38] K. Sokolowski-Tinten, C. Blome, J. Blums, A. Cavalleri, C. Dietrich, A. Tarasevitch, I. Uschmann, E. Förster, M. Kammler, M. Horn-von-Hoegen, and D. von der Linde, Nature **422**, 287 (2003).
[39] D. M. Bates and D. G. Watts, *Nonlinear Regression Analysis and Its Applications*, Wiley Series in Probability and Mathematical Statistics (Wiley, New York, 1988).
[40] A. M. Mamedov and L. Gadzhieva, Soviet Solid State Physics **26**, 2862 (1984).
[41] B. Henke, E. Gullikson, and J. Davis, Atomic Data and Nuclear Data Tables **54**, 181 (1993).
[42] G. E. Jellison, I. Paulauskas, L. A. Boatner, and D. J. Singh, Physical Review B **74**, 155130 (2006).
[43] See Supplemental Material [url] for additional information about our calculations, which includes Refs. [10, 27, 28, 40, 42, 44–53].
[44] C. Paillard, E. Torun, L. Wirtz, J. Íñiguez, and L. Bellaiche, Physical Review Letters **123**, 087601 (2019).
[45] J. H. Jungmann-Smith, A. Bergamaschi, S. Cartier, R. Dinapoli, D. Greiffenberg, I. Johnson, D. Maliakal, D. Mezza, A. Mozzanica, C. Ruder, L. Schaedler, B. Schmitt, X. Shi, and G. Tinti, Journal of Instrumentation **9** (12), P12013.
[46] M. Harmand, R. Coffee, M. R. Bionta, M. Chollet, D. French, D. Zhu, D. M. Fritz, H. T. Lemke, N. Medvedev, B. Ziaja, S. Toleikis, and M. Cammarata, Nature Photonics **7**, 215 (2013).
[47] G. Kresse and J. Furthmüller, Physical Review B **54**, 11169 (1996).
[48] G. Kresse and D. Joubert, Physical Review B **59**, 1758 (1999).
[49] J. P. Perdew, A. Ruzsinszky, G. I. Csonka, O. A. Vydrov, G. E. Scuseria, L. A. Constantin, X. Zhou, and K. Burke, Physical Review Letters **100**, 10.1103/physrevlett.100.136406 (2008).
[50] P. E. Blöchl, Physical Review B **50**, 17953 (1994).
[51] A. Togo and I. Tanaka, Scripta Materialia **108**, 1 (2015).
[52] MTI Corporation, KTaO3 sample data from MTI.
[53] MSE Supplies LLC, KTaO3 Potassium Tantalate Crystal Substrates– MSE Supplies LLC (2022).